ELSEVIER

Physica D 142 (2000) 231–253

PHYSICA D

www.elsevier.com/locate/physd

Dynamical modeling of sub-grid scales in 2D turbulence

Jean-Philippe Laval [a,*], Bérengère Dubrulle [b,c], Sergey Nazarenko [d,e]

[a] *CEA/DAPNIA/SAp L'Orme des Merisiers, 709, F-91191 Gif sur Yvette, France*
[b] *CNRS, URA 2052, CEA/DAPNIA/SAp L'Orme des Merisiers, 709, F-91191 Gif sur Yvette, France*
[c] *CNRS, URA 285, Observatoire Midi-Pyrénées, 14 av. E. Belin, F-31400 Toulouse, France*
[d] *Mathematics Institute, University of Warwick, Coventry, CV4 7AL, UK*
[e] *Department of Mathematics, University of Arizona, Tucson, AZ 85721, USA*

Received 1 November 1999; received in revised form 1 February 2000; accepted 6 March 2000
Communicated by A.C. Newell

Abstract

We develop a new numerical method which treats resolved and sub-grid scales as two different fluid components evolving according to their own dynamical equations. These two fluids are nonlinearly interacting and can be transformed one into another when their scale becomes comparable to the grid size. Equations describing the two-fluid dynamics were rigorously derived from Euler equations [B. Dubrulle, S. Nazarenko, Physica D 110 (1997) 123–138] and they do not involve any adjustable parameters. The main assumption of such a derivation is that the large-scale vortices are so strong that they advect the sub-grid scales as a passive scalar, and the interactions of small scales with small and intermediate scales can be neglected. As a test for our numerical method, we performed numerical simulations of 2D turbulence with a spectral gap, and we found a good agreement with analytical results obtained for this case by Nazarenko and Laval [Non-local 2D turbulence and passive scalars in Batchelor's regime, J. Fluid Mech., in press]. We used the two-fluid method to study three typical problems in 2D dynamics of incompressible fluids: decaying turbulence, vortex merger and forced turbulence. The two-fluid simulations performed on at 128^2 and 256^2 resolution were compared with pseudo-spectral simulations using hyperviscosity performed at the same and at much higher resolution. This comparison shows that performance of the two-fluid method is much better than one of the pseudo-spectral method at the same resolution and comparable computational cost. The most significant improvement is observed in modeling of the small-scale component, so that effective inertial interval increases by about two decades compared to the high-resolution pseudo-spectral method. Using the two-fluid method, we demonstrated that the k^{-3} tail always exists for the energy spectrum, although its amplitude is slowly decreasing in decaying turbulence.

Keywords: Sub-grid scales; Two-fluid simulation; Pseudo-spectral simulation

1. Introduction

Many applications in fluid mechanics require solutions of Navier–Stokes equations at high Reynolds numbers. For flows encountered in aeronautics and engineering, Reynolds numbers can easily reach 10^6. In astrophysics and geophysics they can be even larger. Nowadays, direct numerical simulations (DNSs) on most powerful computers do not reach such Reynolds numbers. For pseudo-spectral methods the problem is that one cannot avoid introducing dissipation even at scales greater than the grid size. The reason for this is a numerical instability which manifests itself in stagnation of energy in small scales and called bottle-neck

* Corresponding author.

0167-2789/00/$ – see front matter
PII: S0167-2789(00)00060-9

instability. To dissipate this energy, a smoothly increasing with wave number dissipation function has to be introduced. To achieve high Reynolds numbers such a dissipation function can be chosen to be of a hyperviscosity type, i.e. a function which is steeper than the real viscosity, but it cannot be made too steep to avoid the bottle-neck instability. Among the various alternatives to DNS is the large Eddy simulation (LES). The idea of the LES is to compute only the large scales and to model the feedback of small scales on the large-scale dynamics. The LES approach is especially popular for computing 3D turbulence, where DNS is practically impossible for high Reynolds numbers (see, e.g. [3] and references therein). Most of the LES schemes, however, are based on phenomenological models for small-scale turbulence and contain adjustable parameters. For 2D turbulence, an LES method was proposed by Sadourny and Basdevant [6].

In the present paper, we implement and discuss a new numerical method for 2D turbulence based on a two-fluid model proposed recently by Dubrulle and Nazarenko [1]. In this model, the large scales and the small (sub-grid) scales are treated as two different components (fluids) described by their own equations. These equations are rigorously derived from the Navier–Stokes equations under the assumption that the large scales produce much stronger velocity field than the intermediate and small scales do. This underlying assumption of the two-fluid method appears to be natural for 2D turbulence because of the energy condensation in large vortices [4,5]. In spirit, the two-fluid model is close to LES, because the small scales are less than the grid size. The dynamical equations are averaged over the small scales and involve only the slow time and coordinate corresponding to the large scales. However, the two-fluid model does not postulate small-scale turbulence but models it with a dynamical equation which does not involve any adjustable parameters. This model conserves both energy and enstrophy, and describes accurately the non-local interaction arising between well-separated scales. It was used to give a simple analytical solution of the interaction between a large-scale dipole vortex and a small-scale turbulence [1], and to derive spectra of non-local 2D turbulence [2].

Yet another related approach in numerical modeling of turbulence, which is also based on velocity decomposition into the large-scale and small-scale components uses the concept of approximate inertial manifolds stemming from the dynamical systems theory [32]. This, essentially statistical, theory gives a slaving law of the small scales as a function of the large scales. Note that the small scales are not slaved in the two-fluid method and they are treated dynamically rather than statistically.

The main goal of this paper is to use the two-fluid method in more realistic situations, where there is no spectral gap separating the large and small scales. Justification of using the two-fluid model for distributions without spectral gap is that intense vortices with the size (in terms of velocity) much greater than the grid cell give a dominant contribution into the dynamics of small sub-grid scales, and intermediate scales may be neglected in the sub-grid scale dynamics. In other words, the sub-grid turbulence is non-local, and the main contribution to the energy and enstrophy fluxes in small-scale turbulence comes from non-local wave number triads having one short leg and two long legs. This situation is indeed observed in high-resolution numerical computations of 2D turbulence [7–9]. To avoid any confusion it is appropriate to remark here that the 2D forced turbulence is indeed local for scales larger than the forcing scale and therefore the $-\frac{5}{3}$ inverse cascade spectrum is observed. We emphasize, however, that it becomes non-local in the enstrophy cascade range at small scales and sub-grid scales in particular. Non-locality assumption works even better for decaying turbulence with no dissipation at low wave numbers because the integral scale of turbulence in this case can be as large as the computational box size at late stages. Of course, neglecting local interactions of sub-grid scales is only an approximation, but this is a much better approximation for 2D turbulence than neglecting the non-local interactions which is done when using the traditional LES approach. The non-locality of 2D turbulence and its relation to the passive advection of small scales resulting in k^{-3} energy spectrum and coherent structures responsible for a steeper spectrum at smaller wave numbers was discussed in [10]. The passive

advection of small scales is the main validity requirement for the RDT (rapid distortion theory) description in 2D. Note, however, that this advection is not truly passive in our approach in that the small scales affect the large scales through the averaged Reynolds stresses, which are taken into account in the two-fluid model.

During the non-local dynamics, the sub-grid energy may not be conserved: it can be transferred to, or be drawn from, the large-scale component. This energy transfer to/from the large-scale component is taken care of in the large-scale equation of the two fluid by a term describing the feedback of the small scales. We use a pseudo-spectral code to compute the large-scale component and we use a particle-in-cell (PIC) method to compute the small scales. Because there is no spectral gap separating the two components, one needs a procedure converting the large-scale fluid into the small-scale one when its scale is approaching the grid size. In turn, when the scale of the small-scale fluid is getting larger than the grid size, one has to convert it into the large-scale component. Such procedure of local conversion of the large scales into the small scales and back is done using a simplified model in order to make the computations cost effective and this part of our numerical method is therefore non-rigorous. Thus, although the two-fluid equations are rigorously derived under the non-locality condition, the whole model (including the conversion between the two fluids) is not rigorous and has to be tested via comparison with high-resolution DNS.

In Section 2, we summarize the two-fluid model and we describe our numerical method in Section 3. In Section 4, we discuss some basic properties of the sub-grid dynamics associated with the particle representation. In Section 5, we consider situations where the large and small scales are separated by a gap, and test our numerical method by comparing with analytical results available for this case. Section 6 is central for the present work. Here, we study three typical problems of the 2D fluid dynamics, decaying turbulence, vortex merger and forced turbulence, and compare the results obtained with the two-fluid method with results obtained by DNS performed at the same and at much higher resolution. We discuss our results and possible applications of our numerical method in Section 7.

2. Two-fluid model

Consider a 2D incompressible inviscid fluid described by the Euler equations

$$\partial_t \omega + \operatorname{div}(\mathbf{v}\omega) = 0, \qquad \operatorname{div}\mathbf{v} = 0, \tag{1}$$

where $\omega = \omega(\mathbf{r}, t) = \operatorname{curl}\mathbf{v}$ is the vorticity. The two-fluid model is derived under the assumption of scale separation and weakness of turbulence compared to the large scales,

$$u = u_{\mathrm{L}} + u_{\mathrm{S}}, \qquad \omega = \omega_{\mathrm{L}} + \omega_{\mathrm{S}} \quad \text{with} \quad u_{\mathrm{L}} \gg u_{\mathrm{S}}, \ \ \lambda_{\mathrm{L}} \gg \lambda_{\mathrm{S}}, \tag{2}$$

where λ is the characteristic scale and S and L label the small-scale and large-scale components, respectively. In this case, Eq. (1) can be decomposed into two equations describing the evolution of the large and small scales [1]. Large-scale component obeys the Euler equation with an additional term describing the influence of small scales,

$$\partial_{\mathrm{T}}\omega_{\mathrm{L}} + (\mathbf{v}_{\mathrm{L}} \cdot \nabla)\omega_{\mathrm{L}} + 2\int (\mathbf{k} \times \nabla)_z \frac{(\mathbf{k} \cdot \nabla)}{k^4} n \frac{\mathrm{d}\mathbf{k}}{(2\pi)^2} = 0. \tag{3}$$

Here, $n(\mathbf{x}, \mathbf{k}, t)$ is the Wigner function of vorticity which corresponds to a density of the small-scale enstrophy in 4D space $(\mathbf{x}, \mathbf{k})$. It is defined in terms of the small-scale vorticity as

$$n(\mathbf{x}, \mathbf{k}, t) = \int \langle \omega_{\mathrm{S}, p+k} \omega_{\mathrm{S}, p-k} \rangle \, \mathrm{e}^{2\mathrm{i}\mathbf{p}\cdot\mathbf{x}} \frac{\mathrm{d}\mathbf{p}}{(2\pi)^2}. \tag{4}$$

The symbol $\langle \cdot \rangle$ denotes an average over the fast time corresponding to the small scales. The Wigner function is a very useful tool for describing interaction of the separated scales in fluids and plasmas, see, e.g. [1,11,12].

The equation for the small-scale component involves $n(\mathbf{x}, \mathbf{k}, t)$. It expresses the fact that total small-scale enstrophy is conserved during the evolution,

$$D_{\mathrm{T}} n = 0 \quad \text{with} \quad D_{\mathrm{T}} = \partial_t + \dot{\mathbf{x}} \cdot \nabla + \dot{\mathbf{k}} \cdot \partial_k,$$
$$\dot{\mathbf{x}} = \mathbf{v}_{\mathrm{L}}, \quad \dot{\mathbf{k}} = -(\mathbf{k} \cdot \nabla)\mathbf{v}_{\mathrm{L}}, \tag{5}$$

where ∂_k is the gradient in the $\mathbf{k}$-space. The large scales act on small scales via changing characteristics of Eq. (5). Small scales in turn, react back on the large scales via the interaction term in (3). The closed system of nonlinearly coupled equations (3) and (5) will be used in this paper as a basis for the two-fluid numerical method described in the next section. Simple analytical solutions of these equations were found for a vortex dipole propagating through turbulence [1] and for the energy spectra of forced and decaying small-scale turbulence [2]. These analytical solutions will be used in the present paper as a reference for testing the numerical method.

3. Numerical method for computing the two-fluid equations

3.1. PIC method for the sub-grid fluid

The small-scale equation (5) is computed by a PIC method which is often used for computing plasmas [13]. This method was also used to solve equations similar to (5) in the case of sound–vortex interaction in an isentropic fluid [14]. The PIC method treats the small-scale component as a large ensemble of particles having coordinates $\mathbf{x}_p(t)$ and momenta $\mathbf{k}_p(t)$, $p = 1, 2, \ldots, N$. Each particle carries a small fraction of the total enstrophy and moves along a trajectory in $(\mathbf{x}, \mathbf{k})$ space computed according to the last two equations of (5):

$$\dot{\mathbf{x}}_p(t) = \mathbf{v}_{\mathrm{L}}(t), \qquad \dot{\mathbf{k}}_p(t) = -(\mathbf{k}_p(t) \cdot \nabla)\mathbf{v}_{\mathrm{L}}(t). \tag{6}$$

The two differential equations (6) are solved via a stable second-order Runge–Kutta scheme. The enstrophy density function $n(\mathbf{x}, \mathbf{k}, t)$ is expressed as a sum of individual particle contributions,

$$n(\mathbf{x}, \mathbf{k}, t) = \sum_{p=1}^{N} \sigma_p(t) S_x(\mathbf{x} - \mathbf{x}_p(t)) \delta(\mathbf{k} - \mathbf{k}_p(t)), \tag{7}$$

where $\sigma_p(t)$ is the enstrophy of particle p and S_x is a function describing the particle shape. For such a decomposition of $n(\mathbf{x}, \mathbf{k}, t)$, the first equation of (5) implies that the enstrophy $\sigma_p(t)$ of each particle does not change during its motion:

$$\sigma_p(t) = \sigma_p(t_0) = \sigma_p. \tag{8}$$

We have chosen the following shape factor for particles:

$$S_x(\mathbf{x} - \mathbf{x}_p) = \begin{cases} 4\dfrac{(\Delta - |x - x_p|)}{\Delta^2}\dfrac{(\Delta - |y - y_p|)}{\Delta^2} & \text{if } \begin{cases} |x - x_p| < \Delta, \\ |y - y_p| < \Delta, \end{cases} \\ 0 & \text{otherwise,} \end{cases} \tag{9}$$

where constant Δ is the particle "size".

At very high wave numbers one has to "dissipate" particles by removing them from the system in order to keep the number of particles at a reasonable level and maintain a low computational cost. As we will see later, such dissipation is typically many orders of magnitude smaller than that in any high-resolution DNS, which allows us to obtain very wide inertial range in our computations. The particle energy, σ_p/k^2, becomes very small when the particle reaches high wave numbers, which means that its initial energy has been transferred to the large-scale fluid via the interaction term. Thus, the particles at high k have no effect on the overall dynamics and can be removed. To be precise, the error associated with removing the particles is very small compared with the error introduced by the other parts of the code. It is also easy to take into account the real viscous dissipation at small scales by reducing the particle strength in time as it was done in [2]. In this paper, however, we will not be interested to study the effect of viscosity.

3.2. Computing the large-scale fluid

The large-scale equation (3) can be solved in various ways. We used periodic boundary conditions and a pseudo-spectral method for the space variables. This method is fast, accurate and easy to implement [15]. The time marching is done in the Fourier space with a stable second-order Adams–Bashford scheme. A

detailed description of the numerical procedure can be found in [16].

The interaction term in (3) is computed in the following way:

$$2\int (\mathbf{k}\times\nabla)_z \frac{(\mathbf{k}\cdot\nabla)}{k^4} n \frac{\mathrm{d}\mathbf{k}}{(2\pi)^2} = 2\{(\partial_{yy}-\partial_{xx})I_1(\mathbf{x},t) + \partial_{xy} I_2(\mathbf{x},t)\}, \tag{10}$$

where

$$I_1(\mathbf{x},t) = \int \frac{k_x k_y}{(k_x^2+k_y^2)^2}\, n(\mathbf{x},\mathbf{k},t)\frac{\mathrm{d}\mathbf{k}}{(2\pi)^2},$$
$$I_2(\mathbf{x},t) = \int \frac{k_x^2-k_y^2}{(k_x^2+k_y^2)^2}\, n(\mathbf{x},\mathbf{k},t)\frac{\mathrm{d}\mathbf{k}}{(2\pi)^2}. \tag{11}$$

Using (7), we have

$$I_1(\mathbf{x},t) = \frac{1}{(2\pi)^2}\sum_{p=1}^{N}\sigma_p \frac{k_{px}(t)k_{py}(t)}{[k_{px}(t)^2+k_{py}(t)^2]^2} \times S_x(\mathbf{x}-\mathbf{x}_p(t)),$$
$$I_2(\mathbf{x},t) = \frac{1}{(2\pi)^2}\sum_{p=1}^{N}\sigma_p \frac{k_{px}(t)^2-k_{py}(t)^2}{[k_{px}(t)^2+k_{py}(t)^2]^2} \times S_x(\mathbf{x}-\mathbf{x}_p(t)). \tag{12}$$

Because we solve our large-scale equation by a spectral method, it is convenient to find the interaction term (10) in Fourier space. In Fourier space, finding the second derivatives with respect to the coordinates will simply correspond to multiplication of Fourier transforms of $I_1(\mathbf{x},t)$ and $I_2(\mathbf{x},t)$ by corresponding wave number components. We then apply a low-pass filter to the interaction term in Fourier space to filter out the high wave number part of the interaction term. The reason for doing so is the fact that the interaction term is derived based on the assumption of scale separation and therefore, it is incorrect for the scales of order of the grid size. On the other hand, the non-local nature of interaction implies smallness of the interaction of sub-grid scales with intermediate scales compared with their interaction with the large scales, and, therefore retaining only the large-scale part of the interaction term is justified. The interaction term describes a force on the large-scale fluid produced by the sub-grid component; it is generally much less than the other terms in the large-scale equation. As we will see further, however, this term is very important for conservation of the total energy of the small-scale and large-scale fluids. On the other hand, the interaction term is shown to be precisely equal to zero at any time if $n(\mathbf{k})$ is isotropic at some particular moment of time [17], e.g. initially. It is interesting that isotropy is not preserved during the evolution, but the developing anisotropy remains of such a kind that the interaction term is still zero at any time. This happens because the positive contribution of some wave numbers is canceled by a negative contribution of the other wave numbers. Note that an initially isotropic spectrum develops into a spectrum with elliptic level lines, and this is a very special kind of anisotropy responsible for the above property.

3.3. Energy conservation

Because of the interaction between the large and small scales, the energy can be transferred between the large-scale and small-scale fluids. However, the total energy of the two fluids is conserved [1]:

$$E_{\text{total}} = E_{\text{L}} + E_{\text{S}} = \int u_{\text{L}}^2\,\mathrm{d}\mathbf{x} + \frac{1}{(2\pi)^2}\int n\,\mathrm{d}\mathbf{k}\,\mathrm{d}\mathbf{x} = \text{const.} \tag{13}$$

In particle representation one can rewrite the small-scale energy as

$$E_{\text{S}} = \frac{1}{(2\pi)^2}\sum_{p=1}^{N}\frac{\sigma_p}{k_p^2}. \tag{14}$$

It was shown in [17] that the energy of the small-scale and large-scale components are conserved separately if n depends only on the absolute value of the wave vector at some moment of time. As we mentioned above, the interaction term in the large-scale equation is equal to zero in this case. We use the energy conservation property as one of the tests in our computations.

3.4. Conversion of the two fluids one into another

In standard DNS approach using pseudo-spectral methods, one has to introduce a dissipation at large

wave numbers to avoid the bottle-neck instability, i.e. piling up the spectrum near the cut-off wave number $k_{\max}$ (corresponding to the grid scale, i.e. the smallest scale resolved by the method). Using a steeper than the regular kinematic viscosity dissipation function (hyperviscosity) allows to suppress the bottle-neck instability and at the same time avoids excessive dissipation at larger scales.

In our method, we do not use any dissipation to stabilize the pseudo-spectral scheme. Instead, we convert the large-scale component into the sub-grid fluid in the vicinity of the cut-off wave number $k_{\max}$. Thus, the spectrum stagnation leading to the bottle-neck instability is avoided by letting the small scales pass the $k_{\max}$ barrier. Then, the sub-grid fluid is evolved according to its own equation which is computed by the PIC method. Note that one does not need any kind of dissipation for stability of the PIC method, and, therefore, one can compute situations with ultra-high Reynolds number (which can be estimated based on the particle removal scale).

The procedure of conversion from the large-scale fluid into the sub-grid one consist of filtering the large-scale vorticity field at wave numbers close to the cut-off wave number $k_{\max}$. Then, we consider the difference between the original and the filtered large-scale spectra of enstrophy and create particles with the same distribution in both coordinate and wave number space. To do this, we first generate an ensemble of particles, each carrying a small equal amount of enstrophy σ and having a momentum $\mathbf{k}$ such that their enstrophy distribution in $\mathbf{k}$-space is the same as the enstrophy spectrum of the converted part of the large-scale component. Second, we compute the difference between the unfiltered and filtered large-scale component in the $\mathbf{x}$-space, and distribute the new particles randomly in the $\mathbf{x}$-space with the weight given by such a vorticity distribution in the $\mathbf{x}$-space. Created this way, the particle ensemble has the same projections into the $\mathbf{x}$-space and into the $\mathbf{k}$-space as would the Wigner function of the converted large-scale vorticity. Direct computation of the Wigner function would be very costly, and the described conversion procedure may be considered as the major approximation made in our numerical model. Besides the enstrophy, the energy is also conserved by our conversion procedure. To achieve a good energy conservation, we adjust the particle $\mathbf{k}$-space distribution in several iterations.

During the evolution, the wave number increases for most of the particles. However, for some particles, the wave number may become lower than its original value and reach the scales which are well resolved by the pseudo-spectral procedure. Because of the low wave number, the energy of such particles is high and, although there are only relatively few of them present in the system, these particles play an important dynamical role. Thus, these low-wave number particles must be converted back into the large-scale component. In our method, this is done by increasing the amplitude of the Fourier component of the large-scale fluid at $\mathbf{k}$ corresponding to the particle's wave number in such a way that this increase would exactly reflect the amount of the particle's energy and enstrophy. We leave the phase of this Fourier component unchanged which makes it easier to conserve energy and enstrophy simultaneously during such a conversion procedure.

3.5. Summary of runs

In Table 1, we summarize for reference different runs which will be discussed in this paper. Below, we describe the relevant details of these runs.

1. The initial stream function of the vortex dipole in run 1 is $\psi(x, y) = (\Gamma/4\pi R)\ln((x^2 + (y - R)^2)/(x^2 + (y + R)^2))$, which is smoothed in the coordinate space to avoid dealing with the point-vortex singularities in the large-scale field. In this run, the particles are initially located on the straight line $x = 0$.
2. In all the runs starting with a random large-scale vorticity the initial energy spectrum is $E(k) = Ck\exp(-(k/k_0)^2)$ with $k_0 = 4$ and $C = 1$.
3. By writing the initial number of particles as a product $N_x N_k$, we mean that we put N_k particles at each of N_x locations in the coordinate space, so that there is a wave number distribution of N_k particles at each of these locations.

Table 1
Description of runs discussed in this paper

Run	Type/Grid	Large-scale initial conditions and forcing	Particle initial conditions and forcing			Interaction term
			Number	Shape **x**	Shape **k**	
1	2F 128^2	Dipole	8×1000	On a line	Isotropic	Off
2	2F 128^2	Random field	2000000	Uniform	Gaussian	Off
3	2F 128^2	Random field	4096×500	Uniform	Isotropic	Off
4	2F 128^2	Random field	0		Forced at $k = 1000$	Off
5	2F 128^2	Random field	16384×36	Uniform	Isotropic	On
6	2F 128^2	Same as run 5	16384×36	Uniform	Anisotropic	On
7	2F 128^2	Random field	0			On
8	2F 256^2	Two vortices	0			On
9	2F 256^2	No field, forced at k=40	0			On
10	HDNS 128^2	Same as run 7	NA	NA	NA	NA
11	HDNS 1024^2	Same as run 7	NA	NA	NA	NA
12	HDNS 256^2	Same as run 8	NA	NA	NA	NA
13	HDNS 1024^2	Same as run 8	NA	NA	NA	NA
14	HDNS 256^2	Same as run 9	NA	NA	NA	NA
15	HDNS 1728^2	Same as run 9	NA	NA	NA	NA

4. In runs 1 and 5, by isotropic particle distribution, we mean that the particle distribution is initially concentrated on the circle $|\mathbf{k}| = k_p = 1000$ in the wave number space as shown on the insert of Fig. 16. In run 3 the particle distribution is initially concentrated on the circle $|\mathbf{k}| = k_p = 100$. By anisotropic initial distribution, we mean a distribution on an 8-shaped curve shown on the insert of Fig. 17.
5. By HDNS we mean a pseudo-spectral method with hyperviscosity k^{16}.

4. Particle dynamics

Let us discuss some basic features of the small-scale dynamics. In the coordinate space, the particles are advected by the local velocity of the large-scale component, see (5). Thus, particles can be mixed in the coordinate space or can be trapped into the large-scale vortices. For the stream function depicted in Fig. 1 (run 1 in Table 1), this property is illustrated in Fig. 2 showing different particle trajectories in the field of a vortex dipole. We see that 1, 2 and 8 are not trapped, whereas particles 3–5 and 7 are trapped and dragged by vortices. Particle 1 is on a special trajectory including a stagnation point, to which it is approaching at a decreasing rate.

Equation for the wave number, i.e. the last equation in (5), is linear with respect to **k**. Therefore, its solution for arbitrary initial wave number **q** can be represented as a linear combination of two solutions obtained for just two different initial wave vectors forming a basis [2,17]. An important consequence of this fact is that the level lines of an initially isotropic distribution of particles $n_0(|q|, \mathbf{x})$ will be transformed from circles to ellipses [1,2,17]. The rate at which

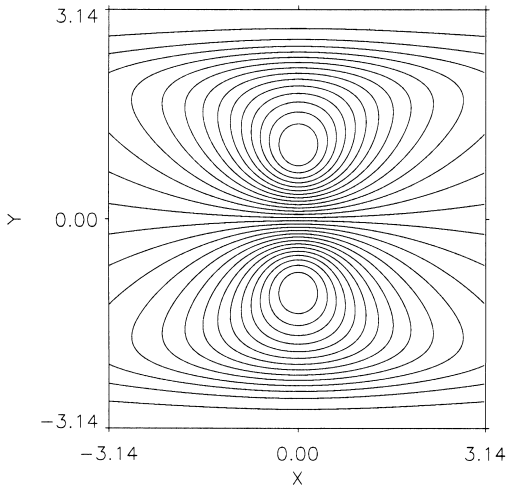

Fig. 1. Stream function of the vortex dipole moving to the right with velocity $u_0 = \Gamma/4\pi R$ (run 1).

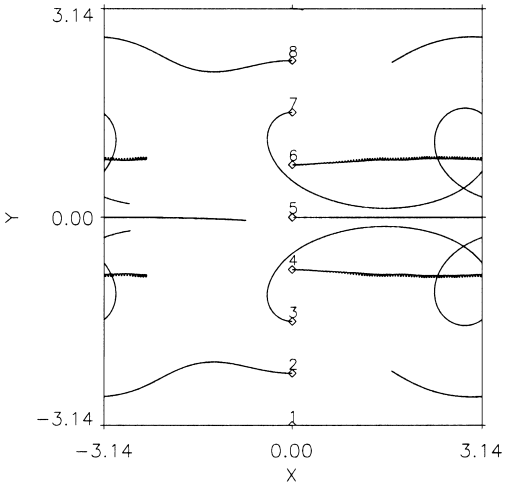

Fig. 2. Particle trajectories in the dipole field (run 1).

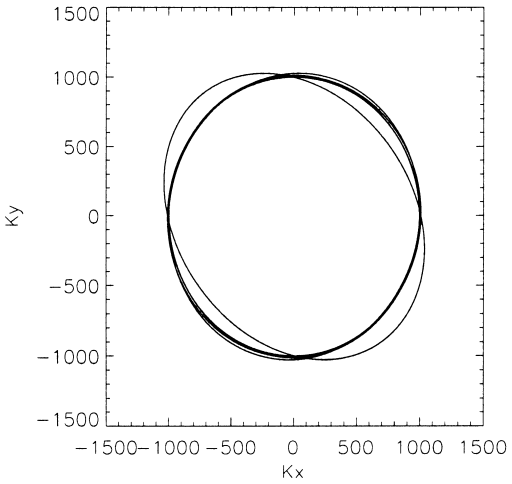

Fig. 4. Wave number distribution of 1000 particles which were initially located at position 4 in the coordinate space (run 1). The circle is only weakly stretched because the shear at the vortex center is less significant.

the ellipse aspect ratio is increasing depends on the local strain of the large-scale field. Figs. 3 and 4 show the time evolution of the ellipses in **k**-space for the particles located on trajectories 3 and 4 in Fig. 2, respectively. We see that initially isotropic distribution becomes anisotropic much slower for the trajectory 4, because it is trapped near the vortex center, where the large-scale motion is approximately just a uniform rotation (plus translation). Note that the ellipse areas are not changing because of the incompressibility of motion in **k**-space [2,17]. This serves as a good test for the PIC code used in our simulations. Conservation of the ellipse areas also means that a wave number increase for some particles will always be accompanied by a wave number decrease for other particles if the initial particle distribution is isotropic.

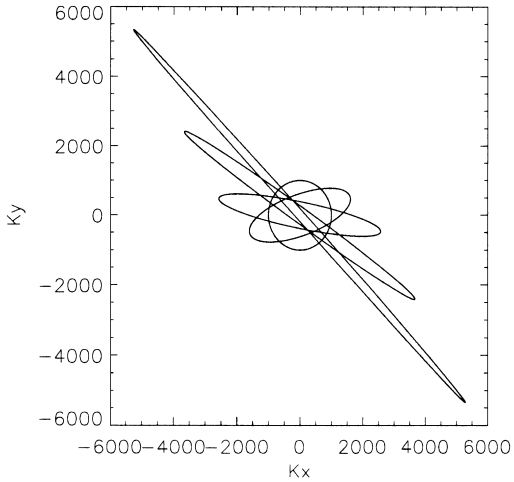

Fig. 3. Wave number distribution of 1000 particles which were initially located at position 3 in the coordinate space. Initial circle becomes an ellipse due to the large-scale shear (run 1).

The second example illustrating properties of the particle dynamics is evolution of a particle ensemble having initial Gaussian distribution in the wave number space and uniform distribution in the coordinate space (run 2 in Table 1). We take random initial distribution of large-scale vorticity for this run. In this simulation, we ignore small scales feedback onto the large-scale fluid (the interaction term) and turn-off the conversion between the small-scale and large-scale components assuming that there is a spectral gap between these two components. Note that under these conditions dynamics of the small-scale vorticity is identical to the passive scalar dynamics in Batchelor's regime (i.e. passive scalar advected by a smooth velocity field).

For random-vorticity initial conditions, a chaotic motion of particles in the coordinate space may be expected [18]. This behavior is illustrated in Figs. 5 and

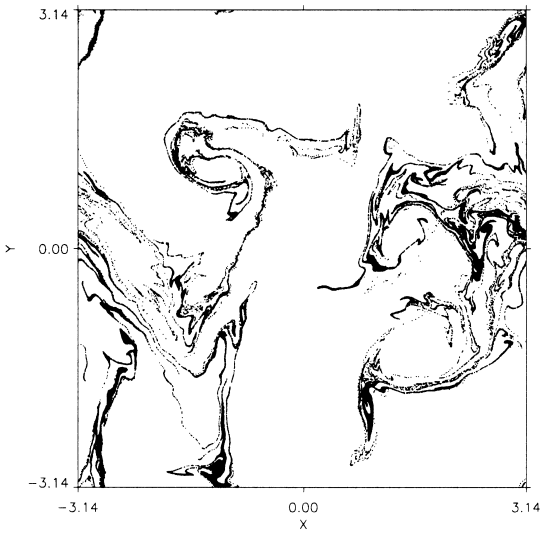

Fig. 5. Coordinates of 50 000 particles initially located in a strip $-\pi \le x \le -\pi + \delta x$ shown at time $t = 5$ (run 2).

6, which show the evolution of 50 000 particles in the (x, y) space. At $t = 0$ these particles were in a narrow strip in the (x, y) space

$$-\pi \le x \le -\pi + \delta x, \qquad -\pi \le y \le +\pi. \tag{15}$$

However, particles cannot cross separatrix and remain

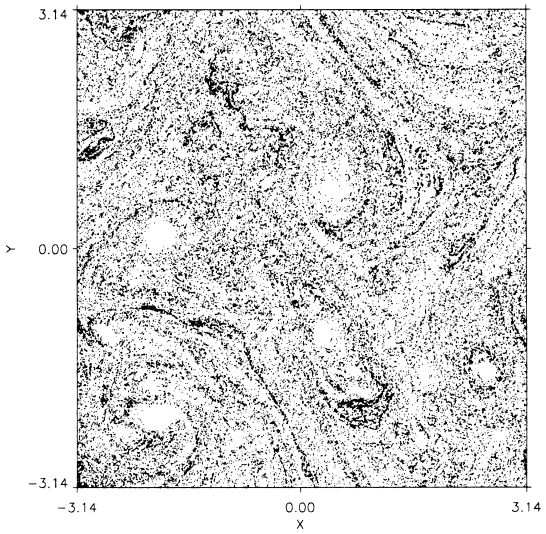

Fig. 6. Position of the same 50 000 particles as in Fig. 5 at $t = 25$. After a long time, particles are mixed by turbulence except at the vortex cores (run 2).

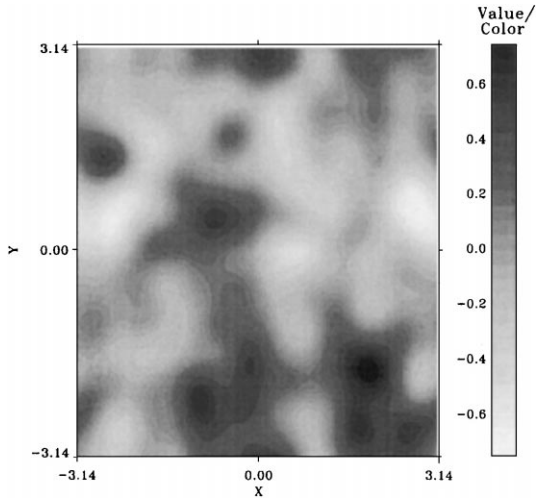

Fig. 7. Initial large-large-scale stream function for run 2. The maximum of the energy spectrum is at $k \simeq 4$.

outside the vortex cores, as clearly seen at late time shown in Fig. 6. Initial large-scale stream function for run 2 is shown in Fig. 7. The initial Gaussian distribution of particles in **k**-space (run 2) is isotropic on an average, but at a later time, smaller vortices in the large-scale component have merged into bigger ones (Fig. 8). (The initial Gaussian distribution is depicted in Fig. 9). This creates some preferred directions of

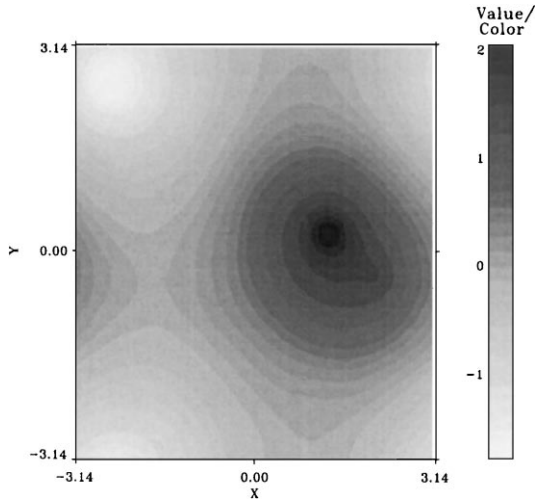

Fig. 8. Large-scale stream function at $t = 50$ for run 2. Small vortices have merged into bigger ones and the large-scale field has become essentially anisotropic.

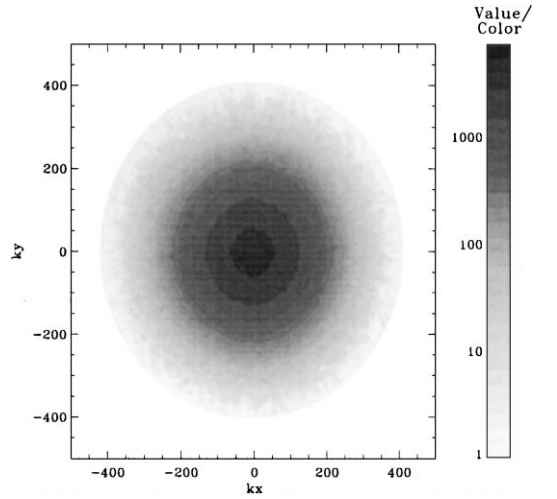

Fig. 9. Initial Gaussian distribution of particles in the **k**-space for run 2.

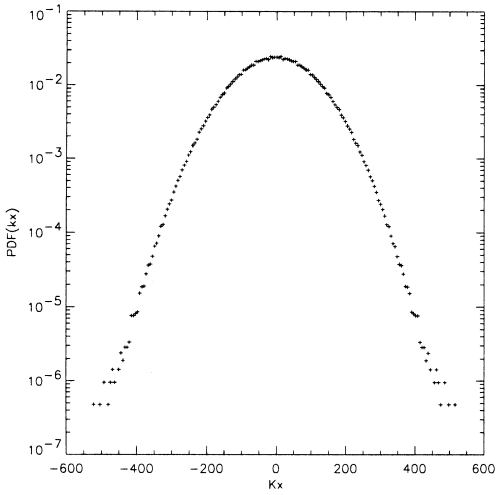

Fig. 11. For run 2, distribution of particles on the k_x axis at $t = 0$ (Gaussian distribution with $\sigma = 100$).

the large-scale shear which are reflected in the particle distribution in the k-space (Fig. 10) because particle wave numbers tend to align with the large-scale shear. Note also a significant spreading of the particle distribution in **k**-space. If we plot the probability distribution of just one wave number component, e.g. k_x, we see that the initial Gaussian profile (Fig. 11) turns later into a distribution close to log-normal (Fig. 12). This result is in agreement with the analytical results of Kraichnan [19] about statistics of derivative of a passive scalar obtained with a rapidly varying velocity field (white noise, delta correlated in time). The deviations with respect to the log-normal distribution observed in the tail of the distribution can be traced to correlations in the large-scale velocity field, which induce a larger intermittency. Such result was also dis-

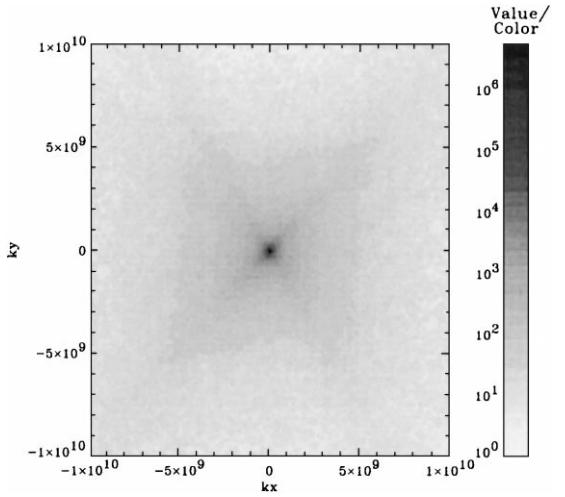

Fig. 10. For run 2, density of particles in the **k**-space at $t = 50$. Note an anisotropy caused by existence of preferential directions for the large-scale shear.

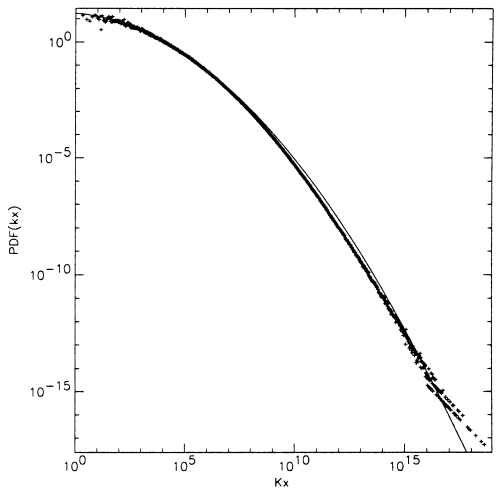

Fig. 12. For run 2, distribution of particles on the k_x axis at $t = 50$. The best fit with a log-normal distribution is shown with a continuous line.

cussed in [19], and can be quantified using the large deviations theory (see, e.g. [20]).

5. Turbulence with a spectral gap

In this section, we continue to study the case when there is a spectral gap between the large-scale and small-scale components. Such a gap has been observed, for example, in the spectrum of horizontal velocity in the atmospheric boundary layer for periods between a few minutes and a few hours, under special conditions [21]. Other situations where the spectral gap is observed in nature were discussed in [22], where an EDQNM (eddy damped quasi-normal Markovian) approach was used to describe 3D turbulence dynamics. For our purpose the spectral-gap case is also important because there exist exact analytical results which may be used to test our numerical model.

First, we will concentrate only on the small-scale dynamics and consider decaying and forced small-scale turbulence. In this part, the large-scale fluid will be completely decoupled from the small-scale component and computed without the interaction term and without converting one fluid into another. This approach is valid for weak small scales which are well separated from the large scales in **k**-space. To suppress the bottle-neck instability, we will have to introduce a hyperviscosity into the large-scale dynamics.

Second, we will consider stronger small scales and narrower spectral gaps to study the feedback of the small scales onto the large-scale fluid. We will use the procedure of conversion between the components to avoid using hyperviscosity in large scales and thereby to improve the conservation of energy and enstrophy. We will also take into account the interaction term for computing the large-scale fluid. Both the conversion procedure and the interaction term will be important, because our main focus in this part will be on studying the energy budget and transfer of energy between the large-scale and small-scale fluids.

5.1. Decaying small-scale turbulence

Let us introduce the small-scale energy spectrum which is obtained by integrating the density of the particle energy over the angle θ (where $\mathbf{k} = (k_x, k_y) = (k\cos\theta, k\sin\theta)$) and over the **x**-space:

$$\hat{E}(k) = \int \frac{n(x, y, k, \theta, t)}{k^2}\, k\, \mathrm{d}\theta\, \mathrm{d}x\, \mathrm{d}y, \tag{16}$$

so that the total energy of the small-scale fluid is

$$E_S = \int \hat{E}(k)\, \mathrm{d}k. \tag{17}$$

Using the particle representation (7), $\hat{E}(k)$ can be written as a sum of the individual particle energies:

$$\hat{E}(k) = \frac{1}{\mathrm{d}k} \sum_{k-\mathrm{d}k/2<|k_p|<k+\mathrm{d}k/2} \frac{\sigma_p}{k_p(t)^2}, \tag{18}$$

where $\mathrm{d}k$ is a small number. $\mathrm{d}k \ll k$, but large enough for having many particles in the interval $k - \frac{1}{2}\mathrm{d}k < |k_p| < k + \frac{1}{2}\mathrm{d}k$.

According to an asymptotical analytical solution for decaying small-scale turbulence obtained in [2], the small-scale spectrum, initially concentrated around some scale $|\mathbf{k}| = k_p$, will tend to a power law shape,

$$\hat{E}(k) \propto k^{-2}.$$

The -2 slope is predicted in a wave number range centered at k_p, which is widening with time. Fig. 13 shows the energy spectrum of freely decaying small-scale turbulence obtained by numerical computation with initial distribution of small scales concentrated on a ring in **k**-space, $n \propto \delta(|\mathbf{k}| - k_p)$ with $k_p = 100$ (run 3 in Table 1). We see that slope -2 is indeed observed in a widening range of wave numbers centered at $k_p = 100$, whereas a steeper slope is observed for higher wave numbers.

5.2. Forced small-scale turbulence

Consider now the case when particles are injected at the circle $|\mathbf{k}| = k_p = 1000$ in **k**-space at a constant rate (run 4 in Table 1). Then, formation of a stationary spectrum is expected for the small-scale turbulence non-locally interacting with the large-scale component [2]. This spectrum has exponent -1 for wave numbers less than k_p and exponent -3 for $|\mathbf{k}| > k_p$. The -1 range corresponds to a constant flux of the small-scale energy to lower wave numbers, and the

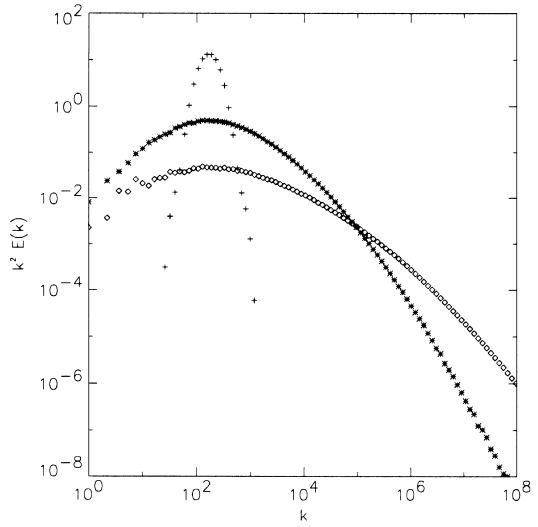

Fig. 13. Compensated energy spectrum of freely decaying small-scale turbulence at three different moments of time obtained in run 3. There is an initial spectral gap between large and small scales in this simulation. Observe formation of a k^{-2} range widening around the initial wave number $k_p = 100$.

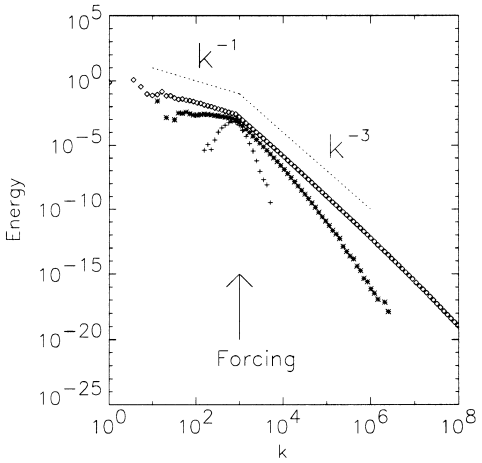

Fig. 14. Energy spectrum of small-scale turbulence forced at $k_p = 1000$ at three different times as obtained in run 4. Turbulence is assumed to be strongly non-local in this case. Observe formation of the k^{-1} spectrum which corresponds to an inverse non-local flux of energy and the k^{-3} enstrophy flux spectrum which extends over a very wide wave number range.

-3 range corresponds to the enstrophy flux. As noted in [2], the spectral exponent for the non-local enstrophy flux spectrum is the same as in case of the local cascade (i.e. -3), whereas the slope corresponding to the non-local energy flux is different from the one corresponding to a local energy cascade (-1 versus $-\frac{5}{3}$).

In our numerical computations of forced small-scale turbulence, we start with no particles and add 16 000 particles every 10 time steps (corresponding to a time $t = 2.5 \times 10^{-3}$). The added particles have a uniform distribution in the coordinate space and are distributed on a circle with a radius $k_p = 1000$ in the **k**-space. Fig. 14 shows the small-scale energy spectrum at three different moments of time. At wave numbers larger than the injection wave number, the spectrum tends to the k^{-3} shape, and at wave numbers smaller than k_p, we observe formation of the k^{-1} spectrum, which agrees with analytical results of Nazarenko and Laval [2].

5.3. Interaction of the small-scale and large-scale fluids

Now we would like to study the nonlinear feedback of the small-scale component onto the large-scale one. For this, we compute the two-fluid equations with both the interaction term and conversion between the two components turned on. In the simulations described in this section, the minimal initial particle wave number is about 20 times greater than the smallest one of the large scales, and the total particle energy is about 20% of the large-scale energy. Fig. 15 shows the evolution of the mean square of the interaction term in runs 5 and 6. We simulate decaying turbulence case with random initial large scales and small scales distributed uniformly in the coordinate space with initial **k**-space distribution on a circle shown on the insert of Fig. 16 (run 5) or on an 8-shaped curve shown in the insert of Fig. 17 (run 6). The principal difference in these two situations is that, in one of them, the initial spectrum of small scales is isotropic, whereas in the other one, the small scales are essentially anisotropic. It was shown analytically in [17] that the energy will be conserved by both small-scale and large-scale components independently of each other in case when the initial small-scale spectrum is isotropic, whereas the energy can be transferred between the components for anisotropic initial spectra. Furthermore, it was shown that the interaction term in the large-scale equation

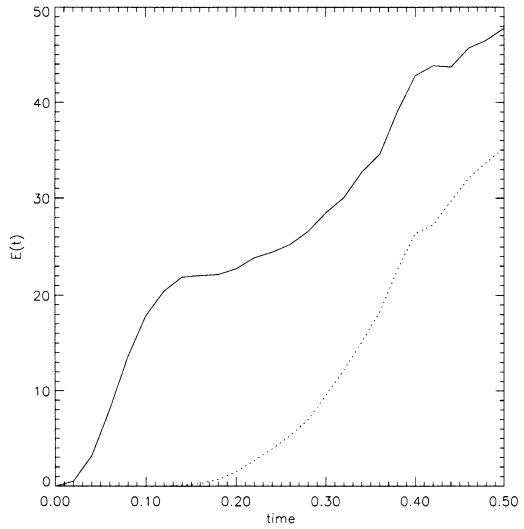

Fig. 15. Mean square of the interaction term as a function of time for the case of initially isotropic small scales (run 5, dashed line) and initially anisotropic small scales (run 6, solid line).

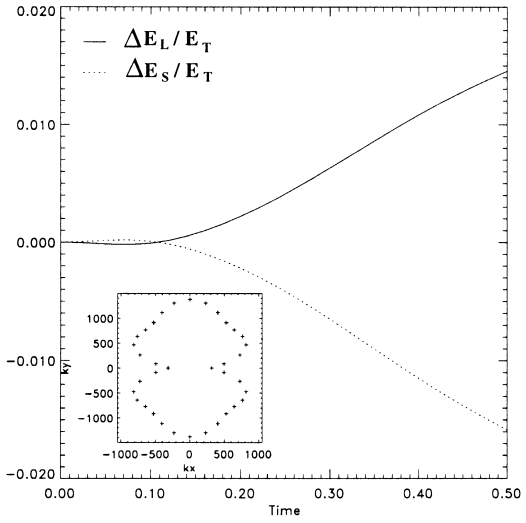

Fig. 17. Variations in the small-scale and large-scale energies, $(\Delta E_S/E_T)$ and $(\Delta E_L/E_T)$ in the case of initially anisotropic small scales ($E_T = E_L + E_S$) (run 6). Insert shows the initial particle distribution in the wave number space.

is identically equal to zero for all times if the initial small-scale spectrum is isotropic in **k**-space and uniform in **x**-space.

Fig. 15 shows the evolution of the mean square of the interaction term in runs 5 and 6. In the beginning, as expected, the interaction term is much stronger for the anisotropic initial small-scale spectrum (run 6) than for the isotropic one (run 5). However, for $t > 0.2$ the magnitude of the interaction terms becomes the same order for both cases. This is because the discretization in x- and k-space with a finite number of particles makes the distribution in the "isotropic" case to be slightly anisotropic, and the role of such an anisotropy grows in time. Fig. 18 shows the large-scale stream function at $t = 0.2$ for run 6, and Fig. 19 shows the interaction term as a function of coordinate for the same run at the same time. We see that the maximum of interaction is strongly correlated with position of strong vortices in the large-scale field.

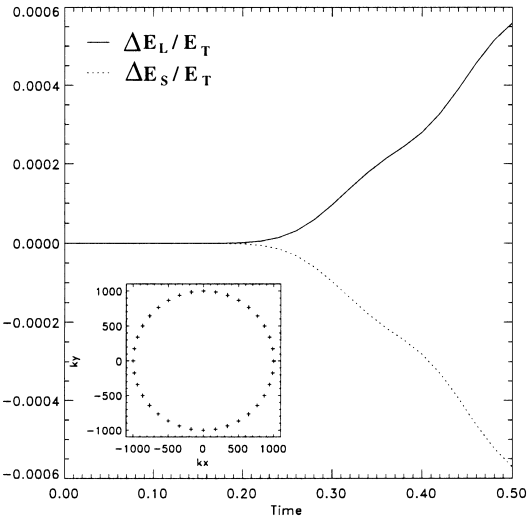

Fig. 16. Variations in the small-scale and large-scale energies, $(\Delta E_S/E_T)$ and $(\Delta E_L/E_T)$ in the case of initially isotropic small scales ($E_T = E_L + E_S$) (run 5). Insert shows the initial particle distribution in the wave number space.

Fig. 16 shows the energy budget for the small and large scales in run 5. As predicted [17], the energy exchange is negligible at the beginning. On the other hand, some energy exchange between the two fluids appears at about $t = 0.3$, which is related with deviations from perfect isotropy in the initial distribution, as explained above. One can see that the exchanged energy is very small compared to the total energy of the system (<0.06%). For the simulation with initially anisotropic small scales (run 6), the energy exchange

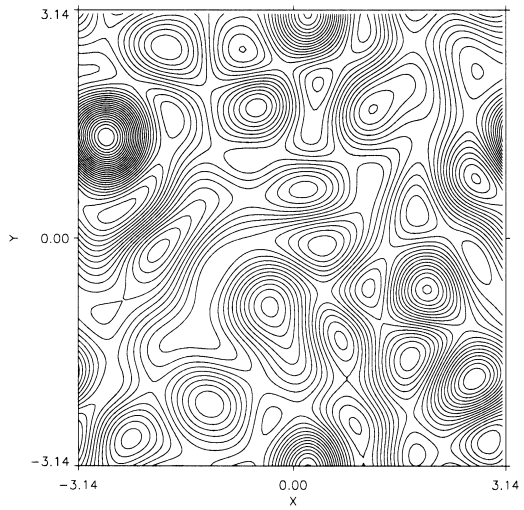

Fig. 18. Stream function of the large-scale vorticity field at $t = 0.2$ for run 6.

starts at a finite rate from $t = 0$, see Fig. 17. As expected, the energy exchange is much greater than in the isotropic case; it is about 2% of the total energy. The error on the total energy conservation is <10% of the energy exchanged.

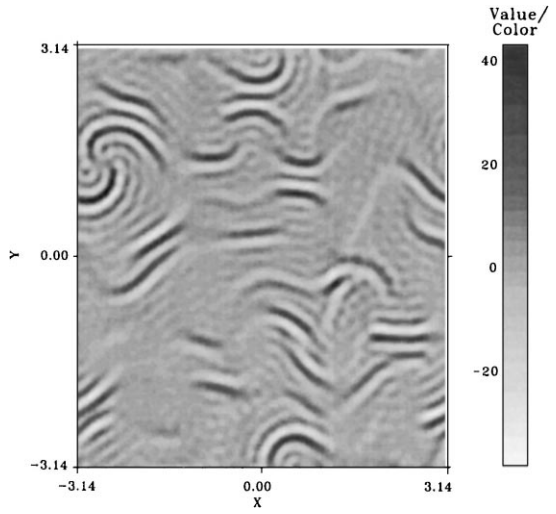

Fig. 19. Interaction term describing the feedback of particles onto the large-scale fluid as obtained in run 6 at $t = 0.2$. Note a strong correlation with positions of large vortices shown in Fig. 18.

6. The two-fluid model versus DNS

In this section, we concentrate on the main goal of this paper, namely using the two-fluid method for solving several typical problems of the 2D fluid dynamics without any spectral gap present in the system. In particular, we will test the performance of the two-fluid numerical method by comparing it to pseudo-spectral DNS with hyperviscosity (HDNS) at the same level of resolution (and approximately same use of computing resources) and at a much higher resolution HDNS. We chose the following three test problems which are frequently computed by other methods: vortex merger, turbulence decay and forced turbulence.

6.1. Decaying turbulence

To simulate decaying 2D turbulence by the two-fluid method, we start with a random initial large-scale component having the energy spectrum shown in Fig. 22 and with no sub-grid (particle) component initially present in the system. Then, evolution of the large-scale component will lead to formation of a k^{-3} tail at high wave numbers corresponding to a down-scale enstrophy cascade. At the time when this tail reaches the cut-off wave number $k_{\max}$, some part of the large-scale component starts being converted into particles by the procedure described in Section 3.4. Note that if we did not convert large scales into particles near $k_{\max}$, we would observe an accumulation of turbulence near $k_{\max}$, because no dissipation (hyperviscosity) is used in the two-fluid method to suppress the bottle-neck instability. Thus, by converting the large scales into particles, we let the enstrophy to pass the $k_{\max}$ barrier and to continue its down-scale flux in the sub-grid fluid computed by the PIC method. The energy budget of the large-scale and small-scale components in this simulation is shown in Fig. 20. The growth of the small-scale energy and an equal energy decrease in large scales seen in Fig. 20 for $t < 5$ corresponds to the conversion of the large-scale fluid into particles when the k^{-3} tail reaches $k_{\max}$. Particles take over the k^{-3} energy distribution and continue it for about three decades more in the sub-grid scale range, as seen in Fig. 23, which

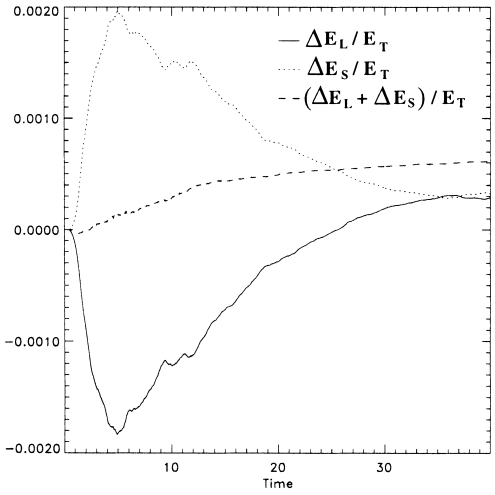

Fig. 20. For run 7, decaying turbulence: small-scale energy E_S/E_T, variations in the large-scale energy $\Delta E_L/E_T$ and the error $(\Delta E_L + E_S)/E_T$ (run 7).

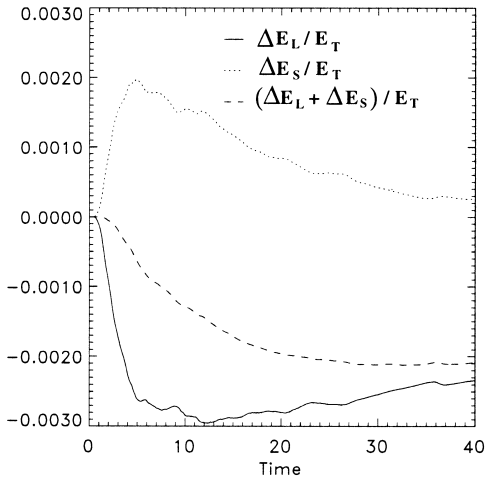

Fig. 21. Decaying turbulence with the interaction term switched off: small-scale energy E_S/E_T, variations in the large-scale energy $\Delta E_L/E_T$ and the error $(\Delta E_L + E_S)/E_T$ (run 7 without the interaction term).

shows the wave number energy distribution for both large-scale and small-scale components at $t = 40$.

It is interesting that after initial growth associated with unsteady formation of the k^{-3} distribution, the small scales transfer their energy back into the large-scale component, see Fig. 20. Such a non-local up-scale energy transfer proceeds with preservation of the k^{-3} shape of the small-scale energy spectrum (the amplitude of which will be of course decreasing). In other words, the energy flux continues to be directed up-scale even when the interaction becomes strongly non-local and there is always a k^{-3} range associated with a down-scale enstrophy flux. The spectral flux of enstrophy slows down because of depletion of the enstrophy reservoir in decaying turbulence, and this corresponds to the decrease of the total amplitude of the k^{-3} spectrum.

Fig. 20 shows also the change in the sum of the energies of the large-scale and small-scale components associated with a numerical error. As we see, the energy non-conservation is very small compared to the total energy of the system. It is also small enough for enabling a reliable analysis of the energy exchanges between the components. To illustrate the importance of the interaction term for conservation of total energy, we performed a simulation of decaying turbulence by the two-fluid method with interaction term switched off. The results for the energy budget in the large and small scales and the numerical error in this run are shown in Fig. 21. One can see that the numerical error is significantly greater in this case than in the case with the interaction term taken into account, and it very quickly becomes comparable to the exchanged amount of energy. The initial large-scale energy spectrum for run 7 is shown in Fig. 22.

As a test for the two-fluid method, we performed two HDNS using a pseudo-spectral method with hyperviscosity starting with identical initial conditions. One of these simulations was performed at the same resolution as the large-scale part of the two-fluid method (128^2) and it required comparable amount of computing resources (typically about 1.5–2 times greater than the CPU time). Another simulation was performed at 1024^2 which requires much greater computational power. Energy spectra obtained in these two HDNS are plotted in Fig. 27 together with the energy spectrum obtained in the two-fluid simulation (sum of the large-scale and small-scale spectra). One can see that the spectrum obtained by the low-resolution HDNS is dissipated by hyperviscosity at much larger scales than both spectra obtained by the high-resolution HDNS and the two-fluid method.

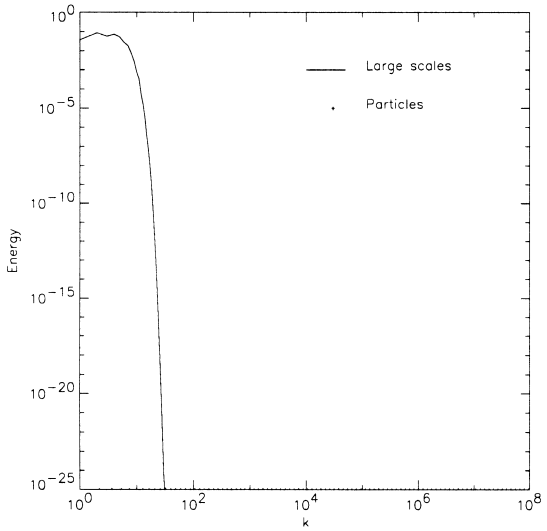

Fig. 22. The initial large-scale energy spectrum for run 7. There are no particles at $t = 0$.

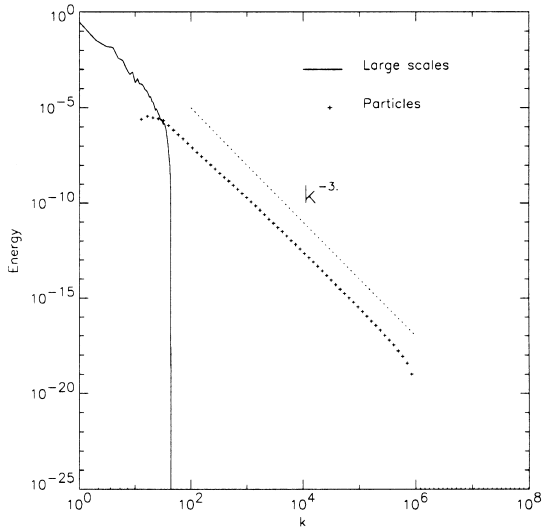

Fig. 23. For run 7, energy spectra of the large-scale and sub-grid (small-scale) fluids in decaying turbulence at $t = 40$. The fluids are converted one into another near $k = 40$, which corresponds to the maximal resolved wave number in this simulation.

The two-fluid method gives a spectrum which is very close to the high-resolution HDNS until the scale where the hyperviscous numerical dissipation makes the HDNS spectrum decay. Furthermore, it continues continuously on slope -3 much further beyond the hyperviscous scale making the enstrophy inertial range about two decades wider than that in the high-resolution HDNS, see Fig. 23. Thus, we see that the 128^2 two-fluid method appears to perform as good as 1024^2 pseudo-spectral method or even better in describing the small-scale turbulence spectra. It is also important to note that the spectrum obtained by the two-fluid simulations is clearly continuous at the cut-off scale $k_{\max} = 42$. Thus, there is a good matching at the interface scale between the two components which are computed by drastically different numerical procedures. Finally, we compared our decaying energy spectra with the "classical" self-similar law of Batchelor [23] in all three cases. We did not obtain a self-similar collapse of the energy spectra in any of the three cases. This is in agreement with a recent detailed numerical study of Bartello and Warn [24], which indicates that Batchelor's similarity hypothesis fails to describe high-order moments of the vorticity distribution. They attribute this failure to the existence of a second rugged invariant, which can be either associated with the support of the vorticity density or the amplitude of the strongest vortices.

From the point of view of LES, it is also important to see whether a particular way of sub-grid scale modeling helps to better describe dynamics of large eddies. Figs. 24–26 show the large-scale vorticity field obtained by the high-resolution HDNS (only 128^2 modes corresponding to the large scales are shown), low-resolution two-fluid method, and low-resolution HDNS, respectively, at $t = 10$. One can see that all three pictures are very similar, so that it is not clear if the large eddy dynamics is simulated better by the two-fluid method than by the pseudo-spectral method (Fig. 27) at equal resolution in this particular case. Similar comparison is somewhat more conclusive in the case of vortex merger problem discussed in the next section.

6.2. Vortex merger

Simulation of merging of two vortices having the same sign is a good test for our two-fluid model because we can compare both the characteristics of large structures like the size and rotation speed of the final vortex, and the small-scale component including vor-

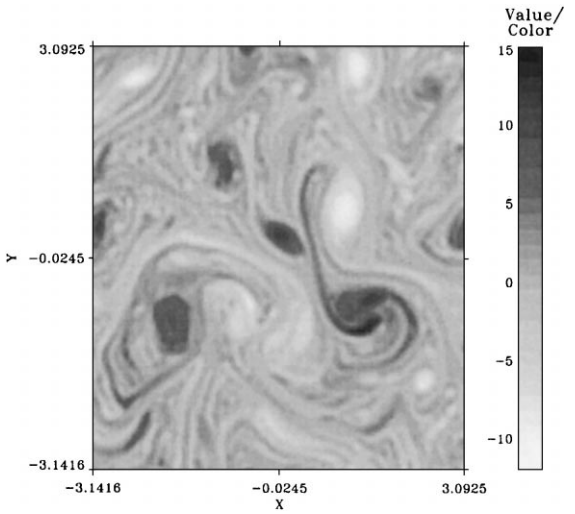

Fig. 24. The large-scale vorticity field in decaying turbulence at $t = 10$ for HDNS 1024^2 (run 11). Only 128^2 modes are shown to retain the same range of scales as in Figs. 25 and 26.

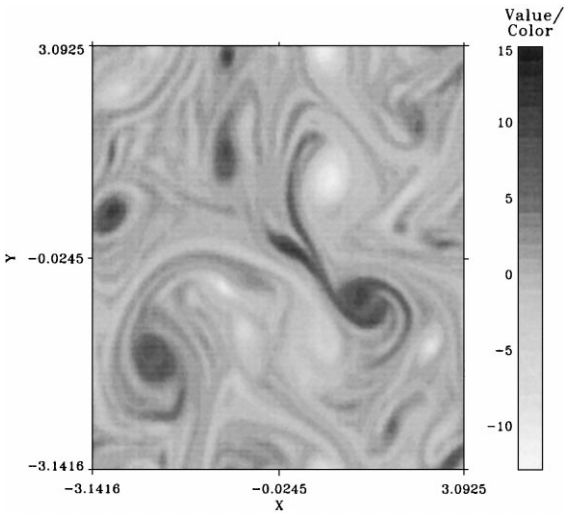

Fig. 26. The large-scale vorticity field in decaying turbulence at $t = 10$ for HDNS on the 128^2 grid (run 10).

ticity filaments. We chose the following initial vorticity field representing the two vortices separated by a distance δ, and with individual vorticity distribution [25]:

$$\omega(r,\theta) = \frac{1}{2}\omega_0 \left\{1 - \tanh\left[\frac{r - R_0}{\Delta}\right]\right\}. \tag{19}$$

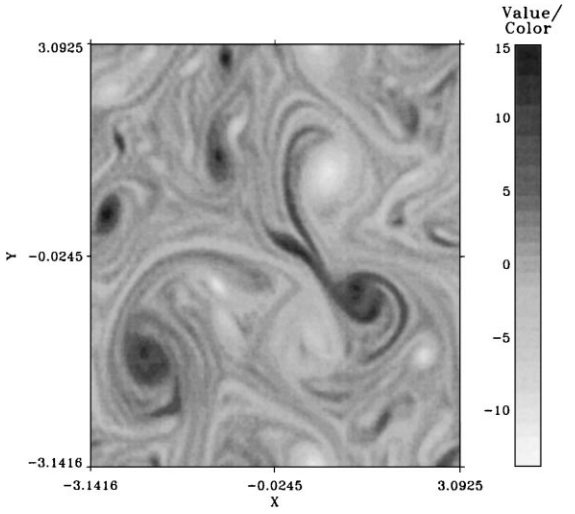

Fig. 25. The large-scale vorticity field in decaying turbulence at $t = 10$ for a two-fluid simulation on the 128^2 grid (run 7).

In our simulations, $R_0 = 0.05 \times 2\pi$, $\omega_0 = 100$, $\Delta = 0.01$ and $\delta = 0.15 \times 2\pi$. The initial vorticity field is shown in Fig. 28, and the corresponding energy spectrum is given in Fig. 29. As in the case of decaying turbulence, we performed three simulations with the same initial conditions: HDNS at 1024^2 and 256^2 resolutions (pseudo-spectral method with hyperviscosity)

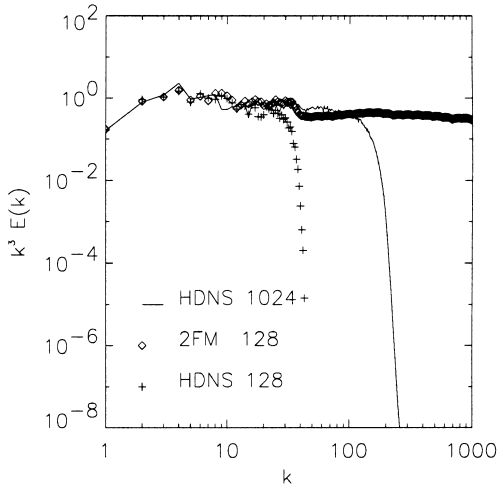

Fig. 27. Compensate energy spectra of decaying turbulence obtained by HDNS 1024^2 (run 11, solid line), HDNS 128^2 (run 10, marked by +) and a two-fluid simulation on the 128^2 grid (run 7, circles).

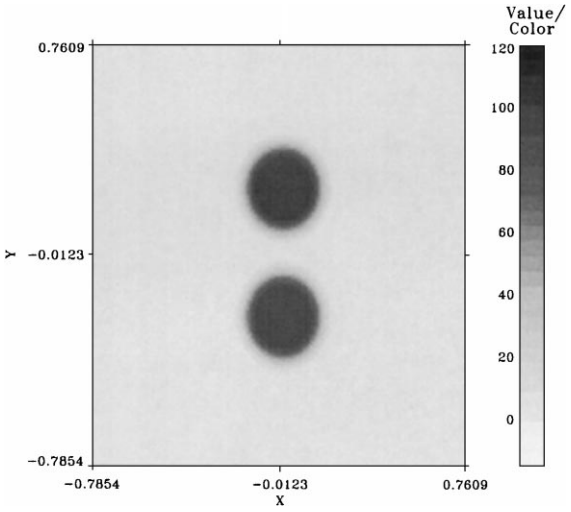

Fig. 28. Initial vorticity field for the vortex merger problem, runs 8, 12 and 13.

and a two-fluid simulation at 256^2 resolution, which correspond to the runs 8, 12 and 13 in Table 1. Typical computing time on a Sun workstation is 6 days, 2 and 4 h for the high-resolution HDNS, low-resolution HDNS and the two-fluid simulation, respectively. The energy spectra obtained by these three simulations are shown in Fig. 33. We see that the low-resolution two-fluid simulation reproduces the result obtained by a high-resolution HDNS very well for all wave numbers up to the numerical dissipation scale of the HDNS method. In contrast, the HDNS performed at the same resolution as the two-fluid simulation exhibits a spectral decay at much lower k because of the hyperviscosity and a lower cut-off wave number. Thus, at least as far as the spectra are concerned, the results obtained by the two-fluid method appear to be reliable even for the scales which are much less than the cut-off scale of the high-resolution HDNS. This is related with almost exact enstrophy conservation built in the two-fluid method, whereas the pseudo-spectral methods must dissipate enstrophy via hyperviscosity for their stability. Note that the spectrum is continuous at the cut-off $k_{\max} = 85$, which serves as a boundary between the resolved and sub-grid fluids computed by completely different numerical procedures.

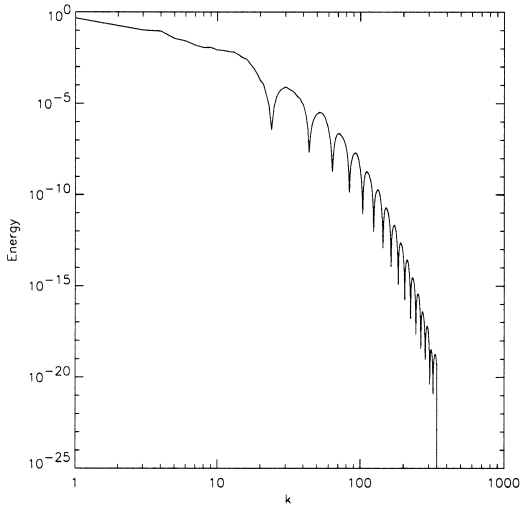

Fig. 29. Initial energy spectrum in the vortex merger problem, runs 8, 12 and 13.

Let us compare now results for the large-scale dynamics in real space obtained by the three different simulations described above. Fig. 30 compares the results for the vorticity field in the central region which is $\frac{1}{16}$ of the total computation domain. For the 1024^2 results, we showed only 256^2 modes corresponding to the large-scale field. Filaments of positive vorticity are well defined in the high-resolution HDNS. One can see that these filaments are better defined in the two-fluid 256^2 simulation than for the HDNS performed at the same resolution. One of the reasons for this result is that excessive hyperviscosity dissipates filaments in the 256^2 HDNS. Another possibly more important reason is that the particles produced at high-gradient regions, associated with filaments, remain a part of the filamentary structure, because both particles and the filaments are advected with the same speed. Remaining on the filaments (see Fig. 32) these particles produce a selective forcing of the large-scale flow at the position of filaments via the interaction term which acts to oppose the diffusion of filaments. Note also that the orientation of the final vortex obtained by the two-fluid method is closer to the 1024^2 simulation than the one obtained by the 256^2 HDNS. Using these differences in orientation and taking into account that the vortex system has made about seven turnovers by the time these differences are observed, one can estimate the numerical error in the mean rota-

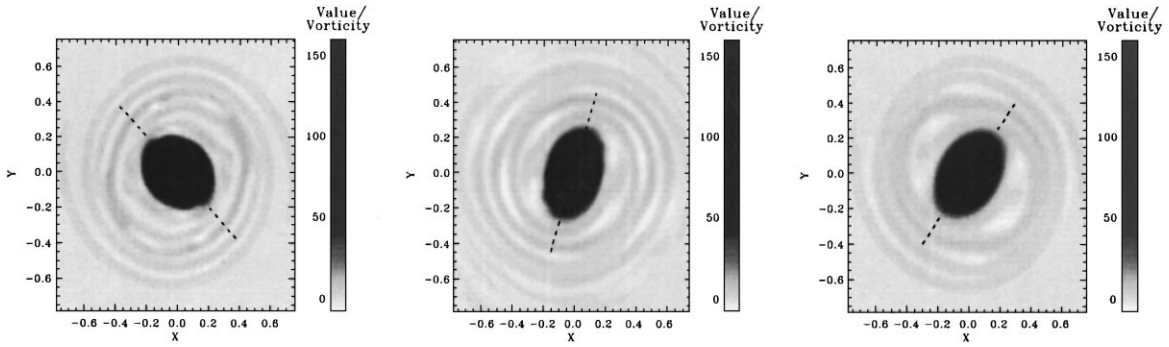

Fig. 30. The large-scale vorticity for the vortex merger problem at $t = 1.5$ as obtained in: (1) HDNS 1024^2 (run 13), two-fluid 256^2 simulation (run 8), and (3) HDNS 256^2 (run 12). Only $\frac{1}{16}$ of the computational area is shown. We retained only 256^2 modes in the figure for HDNS 1024^2 in order to compare the large-scale features only.

tion speed as about 2% for the two-fluid method and 3% for the 256^2 HDNS. One can conclude that the two-fluid method does describe large-scale structures better than the pseudo-spectral method at equal resolution, although these improvements are not as impressive as in description of the small-scale field. In particular, our method does not improve modeling of the sharp edges of the coherent structures because it tends to convert sharp vorticity gradients into particles with partial loss of coherence. Hence, we can describe the spectra much better than the higher momenta and intermittency which is largely caused by the coherent structures.

So far, we discussed the small-scale field only in context of the energy spectra. On the other hand, particles are characterized by distributions in both wave vector and coordinate space, and they contain much richer information about the small-scale field than just spectra. Ideally, the Wigner function describing the particle distributions is invertible and one could recover the small-scale field exactly based on the information about the particle positions and wave vectors. However to create particles, we did not compute directly the Wigner function, which would be too expensive, but used an approximate procedure described in Section 3.4. Nevertheless, the information about the small-scale field contained in particles, although approximate, does contain correlations between different small-scale harmonics. To illustrate this point, we reconstructed the small-scale vorticity field by adding up the contributions of localized wavepackets centered at the particle coordinates $\mathbf{x}_p$ and oscillating in space according to the particle wave vectors $\mathbf{k}_p$. Here, we take wavepackets having two main oscillations in the direction of $\mathbf{k}_p$ and elongated in the transverse to the $\mathbf{k}_p$ direction. The resulting vorticity field for all particles with $k_p < 512$ at $t = 1.5$ is shown in Fig. 31, and this corresponds to the particle locations shown

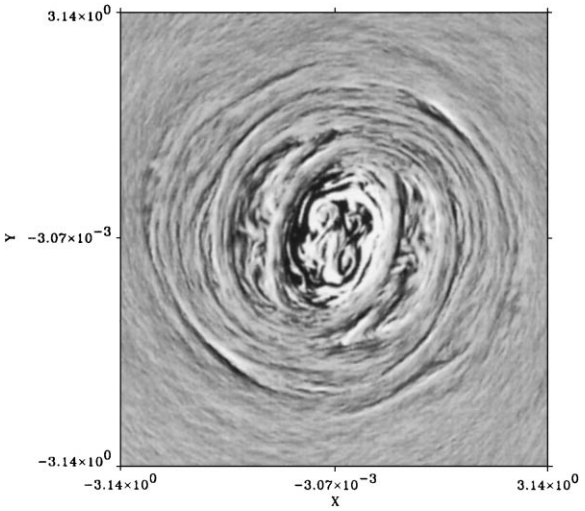

Fig. 31. For run 8, reconstruction of the small-scale vorticity in the vortex merger problem by representing each particle as a vorticity wavepacket and adding up the individual contributions. Here, we considered only particles with $k_p < 512$. Note a coherent filamentary structure of the small-scale field.

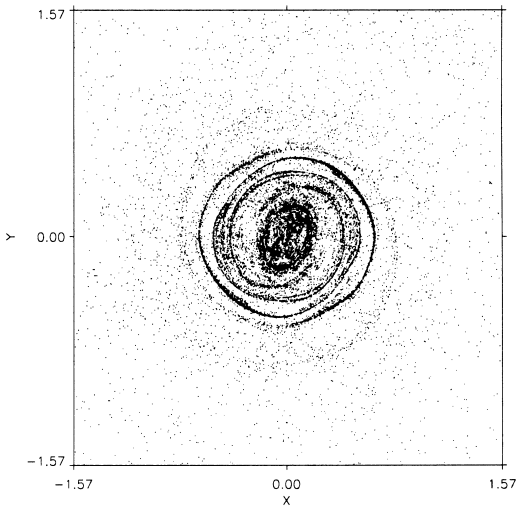

Fig. 32. For run 8, positions of the first 20 000 particles created from the large-scale fluid in the vortex merger problem. Here $t = 1.5$, as in Fig. 31.

in Fig. 32. One can see a very correlated filamentary structure of the vorticity field obtained from the particle distribution.

6.2.1. Forced turbulence

Now let us consider a situation where initially there are no particles and no large-scale field. A force is introduced by keeping the same level of energy for a given wave number, in our case $E = 0.5$ at $k_x = 40$, $k_y = 0$. To obtain a stationary spectrum, a linear friction at large scale is introduced by the term $D_\epsilon = t_\mathrm{d}^{-1} l_\mathrm{d}^{-2} \psi$, where l_d is the box length, t_d the characteristic friction time, and ψ the stream function. Note that by introducing a large-scale friction, we are suppressing, to certain extent, the energy condensation at the largest scale, the process which is important for the two-fluid model. Thus, this set-up provides a harder test of performance for our method.

We perform simulations using the two-fluid method and the pseudo-spectral method, both at 256^2 resolution (Fig. 33), and compare results of these two runs (runs 9 and 14 in Table 1) with the results of a high-resolution HDNS of Babiano et al. [26] who used a 1728^2 pseudo-spectral method with hyperviscosity and the same forcing and large-scale friction as described above (reproduced as run 15). In the case of forced turbulence, the vorticity field is much less

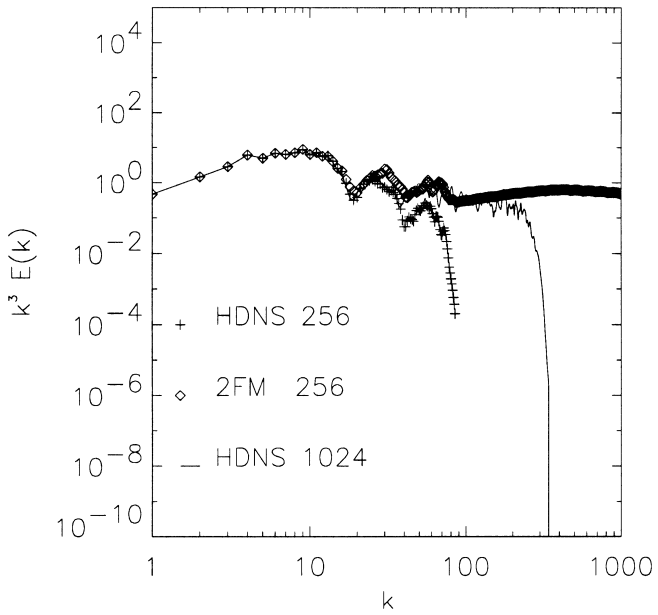

Fig. 33. For runs 8, 12 and 13, compensated energy spectra in the vortex merger problem obtained by the HDNS 1024^2 (solid line), HDNS 256^2 (marked by +) and a two-fluid simulation on the 256^2 grid (circles); runs 13, 12 and 8, respectively.

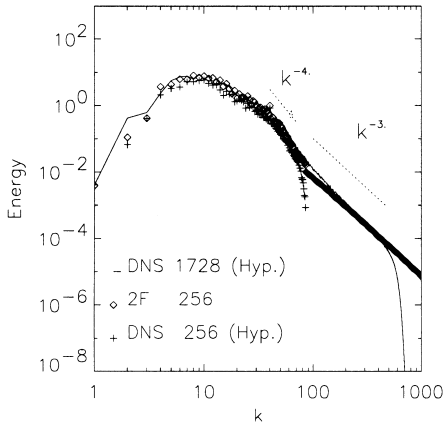

Fig. 34. Energy spectrum of turbulence forced at $k = 40$ which are obtained by HDNS 1728^2 (run 15, solid line), HDNS 128^2 (run 14, marked by $+$) and a two-fluid simulation on the 128^2 grid (run 9, circles).

structured than in decaying turbulence or in the vortex merger problem, and its images in real space do not contain much information which could be used to compare different methods. We will concentrate, therefore, only on the energy spectra, which is shown in Fig. 34. We see that the 256^2 two-fluid simulation gives a very close result to the one of the 1728^2 HDNS for both low and high wave numbers up to the wave numbers where the numerical hyperviscosity makes the HDNS spectrum decay. In contrast, the spectrum obtained by the 256^2 HDNS deviates from the 1728^2 HDNS result not only in high wave numbers, but also in the low k range. Again, one can argue that the enstrophy inertial interval in the two-fluid simulation extends far beyond the cut-off scale of the high-resolution HDNS method.

A slight deviation of the two-fluid simulation from the 1728^2 HDNS is observed around $k = 70$. It is not clear which one of these results is more precise in this region. In the two-fluid result we see a transition from the k^{-3} spectrum at high k to a steeper spectrum closer to the forcing scale. Such a behavior agrees with observations made in [10], where the k^{-3} spectrum was attributed to the passively advected and strained small vortices and the steeper spectrum near the forcing scale was linked to coherent vortices.

Good performance of the two-fluid method in describing forced 2D turbulence confirms validity of the assumption about the non-locality of interaction even in the case when there is a large-scale dissipation which is reducing, to certain extent, the energy condensation at the largest scale. This result is in a good agreement with observation of a strong non-locality of the enstrophy fluxes in forced turbulence with a large-scale dissipation made by Borue [7], who used a high-resolution pseudo-spectral method with hyperviscosity.

7. Conclusion

In this paper, we developed a two-fluid numerical method which treats the resolved and sub-grid scales as two different fluids which are nonlinearly interacting with each other and can be converted one into another near the minimal resolved scale. There are three essential components of the two-fluid method. One of them is the set of equations used to describe evolution of each of the fluids. These equations were rigorously derived in [1] under the assumption of non-locality of interaction in small scales. The second ingredient of the two-fluid model is a PIC scheme to compute the small-scale sub-grid fluid. The last, but not the least, important element of our method is the procedure of conversion of one fluid into another.

By considering turbulence with a gap between large and small scales and by comparing the results with analytical results of Nazarenko and Laval [2], we in fact selectively tested the second element, the PIC discretization of the small-scale field. Indeed, in this part we did not question validity of the two-fluid equations (used to obtain both numerical and analytical results), and we minimized the effect of the conversion procedure (not even using it for some computations) by considering well-separated scales. Our numerical results agree well with the analytical predictions of Nazarenko and Laval [2], which proves effectiveness of using the PIC method to simulate the small-scale equation.

The first and the third components of the two-fluid method were tested by juxtaposition of the results

obtained by this method with results obtained by HDNS performed at the same and at much higher resolution. We saw that the two-fluid method does very well in describing the small-scale part of the spectrum, which verifies the non-locality assumption underlying the validity of the two-fluid equations. We emphasize that our method does not involve any parameters which could be adjusted to make the results look better in comparison with HDNS. (Note that $k_{\max}$ is not an adjustable parameter, it just determines accuracy of the method. Like in usual HDNS, the higher the $k_{\max}$ the more accurate the method is.) We tested the sensitivity of our method with respect to the choice of the cut-off wave number, and we found that sufficiently accurate results may be obtained already for 128^2 resolution. In fact, we believe that the two-fluid method at a low 128^2 and 256^2 resolution describes many features of the small-scale dynamics (e.g. spectra) even better than HDNS at 1024^2 resolution. One of the important features that persistently appears in the two-fluid simulations of different problems is the k^{-3} tail in the energy spectrum. We conclude that the k^{-3} tail is generically present in most of the situations of nearly inviscid 2D dynamics. We think that this tail is not an artifact of our numerical method, whereas steeper small-scale spectra obtained using HDNS are due to the hyperviscous dissipation. It is interesting that the k^{-3} tail persists for a very long time but its amplitude decreases in decaying turbulence, which corresponds to a decreasing enstrophy flux. In this case, an initial small-scale energy increase, associated with fast formation of the k^{-3} tail, is followed by a decrease corresponding to a slow up-scale energy transfer.

We also observed improvements in modeling large scales with respect to the HDNS performed at the same resolution, but these improvements were not as impressive as the ones for the small scales. For example, the difference of the two-fluid results from the high-resolution HDNS for the final vortex orientation in the vortex merger problem is smaller than the deviations associated with the HDNS performed at the same resolution, but these deviations are still comparable. We attribute such deviations to the approximate nature of the conversion procedure which brings about a certain arbitrariness in distributing particles obtained from the large-scale component. Some of the small-scale structures are intrinsically a part of a bigger large-scale vortex, in which case preserving their coherence with this vortex is important. For example, the small-scale structure associated with sharp edges of a large vortex naturally arise near streamline separatrices, and maintaining these structure precisely at the separatrix location is important for preventing a vorticity "leak" to the open streamline regions located beyond the separatrix [27,28]. There is a room for improvement of our conversion procedure which would differentiate between the small scales that belong to a coherent vortex structure from the rest of the small-scale vorticity. One possibility for such an improvement is to perform conversion in the wavelet space where the coherent structures are clearly distinguishable [29]. In this approach, the scale at which the conversion is performed would vary with coordinate (in contrast with a fixed scale used in this paper). Another possibility is to use the "contour surgery" method to describe the large-scale fluid [30]. In this approach, the small-scale fluid would be created from the long and thin filaments, which are cut-off by the "surgery" procedure. One of course would have to develop a procedure modeling the small scale feedback onto the large vortices which would be suitable for this method.

Finally, we would like to mention that there are quite a few types of fluids where the use of the two-fluid approach would be justified. Recall that the underlying assumption of the two-fluid method is that the small-scale dynamics is non-local and can be described by linear equations. The small scales can include not only vorticity, but also a wave component. In fact, the first application of the two-fluid approach was to compute the sound–vortex interaction problem in which the small scales were short acoustic waves (ultrasound) [14]. Further, the first derivation of the two-fluid equations was done for the β-plane model for geophysical fluids where the interaction is typically non-local [12], but no numerical computation of these equations has been done yet. The non-locality assumption is likely to be valid for MHD turbulence, and it was used by Kraichnan [31] to derive the $k^{-3/2}$ energy spectrum of MHD turbulence. In this case, the

small-scale (sub-grid) fluid would be composed of an Alfven wave distribution.

Acknowledgements

We thank M. Meneguzzi for providing us with a copy of his 2D spectral code, and for numerous advice and discussions about the present work. We are grateful to A. Babiano for providing us a field at high resolution and for suggestions. The high-resolution simulations were performed on the Cray C94 of IDRIS and the Cray C90 of the CEA Grenoble.

References

[1] B. Dubrulle, S. Nazarenko, Physica D 110 (1997) 123–138.
[2] S. Nazarenko, J.-P. Laval, Non-local 2D turbulence and passive scalars in Batchelor's regime, J. Fluid Mech., in press.
[3] C. Fureby, et al., Phys. Fluids 9 (1997) 1416.
[4] L. Smith, V. Yakhot, Phys. Rev. Lett. 71 (1993) 352.
[5] V. Borue, Phys. Rev. Lett. 72 (1994) 1475.
[6] R. Sadourny, C. Basdevant, Comput. Rend. Acad. Sci. Paris, Serie II 292 (1981) 1061.
[7] V. Borue, Phys. Rev. Lett. 71 (1993) 3967.
[8] K. Ohkitani, Phys. Fluids A 2 (1990) 1529.
[9] M.E. Maltrud, G.K. Valis, Phys. Fluids A 5 (1993) 1760.
[10] K.G. Oetzel, G.K. Vallis, Phys. Fluids 9 (1997) 2991.
[11] A.M. Rubenchik Izv. Vuzov. Radiofizika 17 (1974) 922.
[12] A.I. Dyachenko, S.V. Nazarenko, V.E. Zakharov, Phys. Lett. A 165 (1992) 330.
[13] C.K. Birdsall, A.B. Langdon, Plasma Physics via Computer Simulation, McGraw-Hill, New York, 1985.
[14] S.V. Nazarenko, N.J. Zabusky, T. Scheidegger, Phys. Fluids 7 (1995) 2407.
[15] D. Gottlieb, S.A. Orszag, Numerical Analysis of Spectral Methods: Theory and Applications, SIAM, Philadelphia, PA, 1977.
[16] M.E. Brachet, M. Meneguzzi, H. Politano, P.L. Sulem, J. Fluid Mech. 194 (1988) 333.
[17] S. Nazarenko, N. Kevlahan, B. Dubrulle, J. Fluid Mech. 390 (1999) 325.
[18] J.M. Ottino, The Kinematics of Mixing: Stretching, Chaos, and Transports, Cambridge University Press, Cambridge, 1989.
[19] R.H. Kraichnan, J. Fluid Mech. 64 (1974) 737.
[20] U. Frisch, Turbulence, Cambridge University Press, Cambridge, 1995.
[21] I. Van der Hiven, J. Meteorol. 14 (1957) 160.
[22] A. Pouquet, U. Frisch, J.P. Chollet, Phys. Fluids 26 (1983) 877.
[23] G.K. Batchelor, Phys. Fluids 12 (Suppl. II) (1969) 233.
[24] P. Bartello, T. Warn, J. Fluid Mech. 326 (1996) 357.
[25] A.H. Nielsen, et al., Phys. Fluids 8 (1996) 2263.
[26] A. Babiano, B. Dubrulle, P. Frick, Phys. Rev. E 55 (1997) 2693.
[27] B. Legras, D. Dritschel, J. Comput. Phys. 104 (1993) 287.
[28] A. Mariotti, B. Legras, D. Dritschel, Phys. Fluids 6 (1994) 3954.
[29] M. Farge, N. Kevlahan, V. Perrier, E. Goirand, Proc. IEEE 84 (1996) 639.
[30] D. Dritschel, Comput. Phys. 77 (1988) 240.
[31] R. Kraichnan, Phys. Fluids 8 (1965) 1385.
[32] T. Dubois, F. Jauberteau, R. Temam, Comput. Meth. Appl. Mech. Eng. 159 (1998) 123–189.